International Journal of Impact Engineering 208 (2026) 105525



Contents lists available at ScienceDirect

International Journal of Impact Engineering

journal homepage: www.elsevier.com/locate/ijimpeng



Dynamic behaviour of functionally graded lattice structures with short carbon fibre reinforcement

Piyapat Jameekornkul, Ajit Panesar *

IDEA Lab, Department of Aeronautics, Imperial College London, SW7 2AZ UK

ARTICLE INFO

Keywords:
Lattice structure
Functional grading
Fibre-reinforced AM
Dynamic behaviour

ABSTRACT

Lattice structures are being increasingly explored due to advances in additive manufacturing (AM). However, their adoption in impact applications is hindered by an insufficient understanding of their dynamic behaviour, particularly for composite and functionally graded (FG) lattices. This study presents the first systematic investigation that concurrently evaluates multiple design parameters, including cell topology, grading strategy, fibre reinforcement, and loading conditions, on the dynamic response of AM lattices. Lattice specimens made from nylon and carbon fibre-reinforced nylon were tested under intermediate strain rates ranging from 22 to 79 s^{-1} using drop-weight impact. The results indicate that both stretching-dominated and bending-dominated architectures retained their characteristic failure modes across the tested strain rates, with the latter exhibiting greater strain rate sensitivity. FG lattices outperform their ungraded counterparts in energy absorption by at least 15.2 %, with fibre reinforcement providing an additional enhancement of up to 37.5 %. The experimental results align well with the Cowper–Symonds model and highlight the combined influence of material and lattice design on rate-dependent performance. The findings and insights gathered pave the way for designing high-performance AM lattices for energy absorption applications.

1. Introduction

Lattice structure are widely recognised for their high strength-to-weight ratio and superior specific energy absorption, making them ideal for lightweight and impact-resistant applications [1]. Extensive research has focused on enhancing their mechanical performance through geometric design and material distribution [2,3]. Gibson and Ashby's foundational work [4,5] identified relative density as a key design parameter governing lattice behaviour. This laid the foundation for functionally graded (FG) lattices, which spatially vary relative density to tailor stiffness, failure modes, and energy absorption. Beyond relative density, additional factors such as cell size [6], topology [7], material composition [8], hybrid designs [9,10], nature-inspired [11,12], and fractal arrangements [13,14] have also been explored to improve structural responses and address limitations in lattice structures, such as manufacturability and stiffness–toughness trade-offs [15].

Despite advances in lattice design, most experimental studies have focused on quasi-static conditions [16], limiting their applicability in crash and ballistic scenarios where dynamic loading dominates [17]. Strain rate sensitivity, commonly used to compare quasi-static and dynamic responses, has primarily been assessed at the extremes: quasi-static ($< 10^{-2}\ s^{-1}$) and high strain rates ($> 10^{3}\ s^{-1}$). Meanwhile, the intermediate or transitional regime (1-100 s^{-1}), which is highly relevant for practical impact scenarios such as tool drop or sporting equipment, remains significantly understudied [18]. Reviews of AM lattice research [1,19] have covered over 100 studies, yet less than 15 % have investigated intermediate strain rate conditions (e.g. [20,21]), and even fewer have explored FG designs (e.g. [22–25]). Moreover, the influence of strain rate on energy absorption in AM lattices remains inconclusive. Harris et al. [26] observed that the hybrid honeycomb exhibited peak SEA at intermediate rates, consistent with findings on FG Octet lattices [22]. Conversely, a monotonic increase in SEA with strain rate in 316 L gyroid lattices was reported by Li et al. [27]. Although early studies suggest that FG designs can alter deformation modes and enhance energy absorption, the combined effects of strain rate and design parameters remain insufficiently explored.

Furthermore, most studies addressing strain rate sensitivity have focused on metallic lattices [19]. However, growing evidence suggests that the dynamic behaviour of lattices also influenced by the base material properties [28,29]. Polymer-based composites, due to their

* Corresponding author.
E-mail address: a.panesar@imperial.ac.uk (A. Panesar).

https://doi.org/10.1016/j.ijimpeng.2025.105525
Received 17 May 2025; Received in revised form 28 August 2025; Accepted 2 September 2025
Available online 4 September 2025
0734-743X/© 2025 The Author(s). Published by Elsevier Ltd. This is an open access article under the CC BY-NC-ND license (http://creativecommons.org/licenses/by-nc-nd/4.0/).

inherent viscoelasticity, may exhibit distinct responses under dynamic loading. Several prior works have highlighted the benefits of carbon fibre (CF) reinforcement in AM lattices: Quan et al. [30] illustrated the CF in honeycomb structure helped inhibit the crack propagation, and Zhou et al. [31] reported superior SEA and compressive strength of composite lattices compared to pure Nylon. Despite these promising results, dynamic characterisation of composite lattices remains limited, mostly focusing on carbon nanotube architectures [32], self-sensing performance [33] and sandwich structures [34]. As material extrusion (MEX) continues to mature as a viable technique for fabricating complex composite parts [35,36], further investigation into the dynamic behaviour of polymer-based composite lattices has become both feasible and necessary. In particular, the role of carbon fibre reinforcement in governing strain-rate sensitivity of lattices remains largely unexplored.

Previous studies have often examined key parameters (e.g. material, lattice architecture, and strain rates) in isolation, thereby limiting understanding of their combined influence on lattice behaviour and hindering the development of effective design strategies for dynamic applications. To address this gap, the study provides the first systematic evaluation of the dynamic response of AM polymer lattices under intermediate strain rates (1–100 s^{-1}), with key contributions outlined in Table 1 and supporting literature reviewed in Appendix A. A series of drop-weight impact tests investigates how grading strategies (i.e. density and cell size), cell topology, printing orientation, strain rate, impact energy, and fibre reinforcement influence failure mechanisms and energy absorption. Results are compared with quasi-static baselines and interpreted using an analytical plasticity model to assess strain rate sensitivity, with fibre-reinforced and unreinforced lattices directly compared to clarify the role of reinforcement in rate-dependent behaviour.

2. Methodology

2.1. Design of lattices

Lattices were designed using LatTess (Lattice Tessellation), an in-house tool developed as described in [40,41]. Two topologies, Body-Centred Cubic (BCC) and Schwarz-Primitive (SP), were selected to represent bending- and stretching- dominated behaviours, respectively. The BCC lattice, a strut-based structure, is generally regarded as bending-dominated according to Maxwell's criterion [42]. Although tension-dominated response has been reported in BCC lattices made from PA12 [43], the conventional classification is adopted here for consistency with prior comparative studies. The relative density of BCC lattices is governed by the strut diameter. The SP lattice is a surface-based Triply Periodic Minimal Surface (TPMS) structure, defined by an isosurface offset from a zero-level implicit function [44], where the isovalue t controls the solid volume fraction. Unless otherwise stated, relative density (ρ) refers to the ratio of the solid volume of the lattice to that of its bounding box.

Table 1
Summary of key research gaps and how they are addressed in this study.

Research Area	State of the Art	Research Gap	Addressed in This Study
Dynamic behaviour	Most existing works focus on high strain rates [37,38] or quasi-static conditions [6]	Intermediate strain rate range (1–100 s^{-1}) is largely unexplored	✓ First systematic evaluation of AM lattice structures under intermediate strain rates
Composite polymer-based lattices	Carbon nanotubes [32] and 2D lattice [39]	Dynamic response of composite lattices remains poorly understood	✓ Fibre alignment and integration effect on lattice's failure mode and strain rate sensitivity
Functionally graded	Existing studies typically vary only one factor (e.g. density) and use a single cell type (See Appendix A	No systematic comparison	✓ Direct comparison of grading type, severity and unit cell under impact

The lattice geometry consists of a $4 \times 4 \times 4$ tessellation forming a cube with an edge length of $L = 20mm$. A unit cell (UC) layer refers to a full one UC-height layer on the XY plane (Fig. 1). Ungraded and graded lattice designs, along with the print direction (z-axis), are shown in Fig. 1. For density gradation, ρ was linearly varied along the z-direction from ρ_{min} to ρ_{max}, as expressed in Eq. (1), while maintaining a constant average density of $\rho_{avg} = 0.5$.

Cell size gradation was implemented following the method proposed in [6,7]. Each lattice was equally divided into three sections along the z-axis, where a base consists of 3 UCs per edge length and increasing linearly 5, 7, or 9 UCs at the top surface. A Sigmoid function was used to define the transition zone between these regions to ensure smooth morphing of cell size (Fig. 1). Cell-size grading was applied only to SP lattices, as their surface-based geometry enables topologically continuous transitions. Meanwhile, truss-based BCC architecture is susceptible to discontinuities due to abrupt changes in nodal connectivity. Other stretching-dominated truss-based topologies (e.g., Octet, FCC) were excluded from this study for similar reasons, though they may serve as valuable intermediate structures for future comparisons between surface- and truss-based architectures.

$$\rho(z) = \rho_{min} + \Delta\rho\left(1 - \frac{z}{L}\right) \tag{1}$$

2.2. Specimen fabrication and characterisation

All specimens were fabricated using a Markforged Mark Two 3D printer [45] with Eiger slicer software, employing uniform printing parameters: 0.1 mm layer height, 100 % solid infill, and two wall layers. Temperature and other process settings followed the default configuration [46]. Unlike powder-based AM, the MEX process eliminates concerns of material entrapment in enclosed regions, enabling the fabrication high-density lattice structures ($\rho > 0.5$), such as $SP^{g}_{0.2-0.8}$ shown in Fig. 1.

Two materials were used: Nylon (PA) and Onyx, a composite comprising chopped carbon fibres (CF) embedded within the same PA matrix [47]. To quantify the carbon fibre volume fraction (CF-VF), thermogravimetric analysis (TGA) was conducted at a heating rate of 10 °C/min up to 700 °C, and the results were compared with reported values [48]. To reduce moisture-related variability, all feedstocks and printed specimens were sealed and oven-dried for a minimum of four hours prior to printing and testing.

Part quality was assessed at both micro- and macro-scales. Microscopy was used to evaluate CF orientation and distribution within Onyx filament. Dimensional accuracy was verified using a digital scale and vernier calliper, and all lattice structures were visually inspected for defects such as cracks or incomplete struts that may compromise mechanical performance.

2.3. Experimental setup

Low-velocity impact tests were performed using the drop-weight method, as other standard tests such as Izod or Charpy require dimension-specific specimens, which are unsuitable for lattice structures. An Instron CEAST 9350 drop-weight tower equipped with a 90 kN load cell and a 100 mm diameter impactor was used. The specimen was placed on a steel plate, and a 26.1 kg impactor was released from predefined heights to achieve impact energies (E_i) ranging from 15 J to 90 J (Table 2). Data acquisition was triggered upon initial contact between the impactor and specimen, with force and time signals recorded at a sampling rate of 50 kHz. Deformation behaviour was captured using a

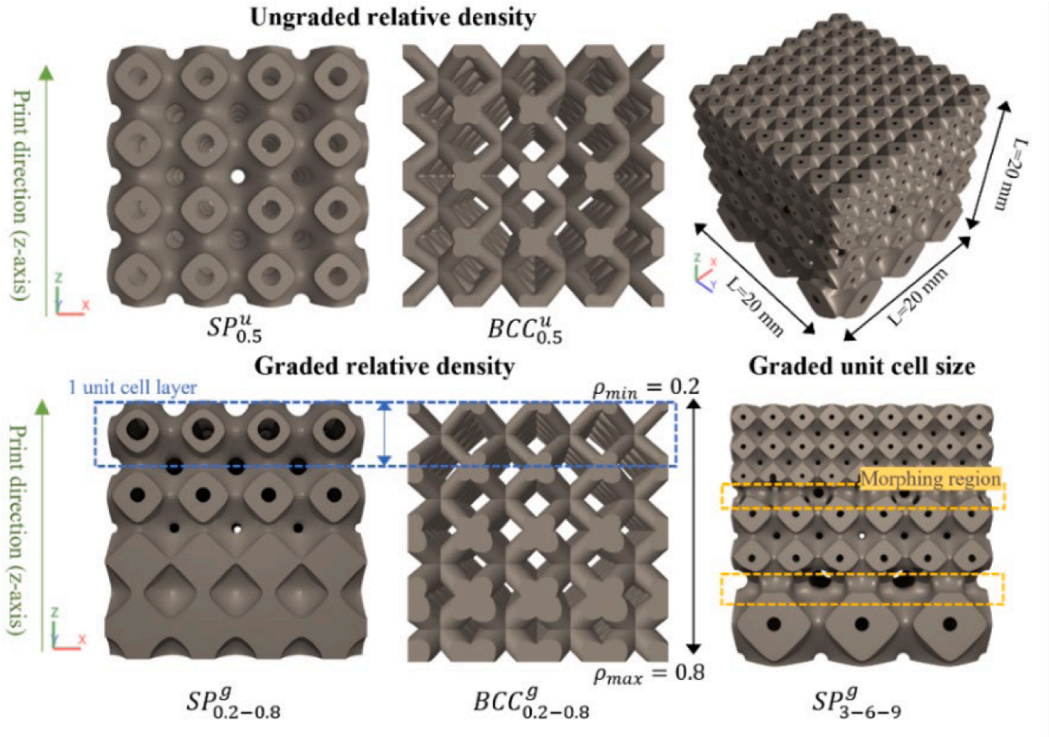


Fig. 1. Lattice structure's dimension and examples of graded specimens.

Table 2
Impact energy levels and associated impactor properties.

Impact energy level	E_i [J]	m_i [kg]	v_i [m/s]	h_i [mm]
Low	15	26.1	1.07	59
Intermediate	45	26.1	1.96	195
High	90	26.1	2.77	390

Note: E_i – impact energy; m_i – impactor mass; v_i – impact velocity; h_i – drop height.

Phantom high-speed camera operating at 50,000 fps. Impactor velocity was calculated from frame-by-frame pixel tracking and time intervals (via PCC Phantom software [49]), then validated against photocell measurements. All values were within ±5 % of the nominal velocity in Table 2.

Testing procedures, including the calculation of striker displacement $\delta(t)$, velocity $v(t)$ and absorbed energy $E_a(t)$, were based on ASTM D7136 standard for drop-weight impact testing of composite laminates [50], with modifications to the support fixture and striker plate to accommodate the lattice geometry. To ensure accurate force measurement, key setup parameters such as load cell position and the mass ratio between the load cell and the drop weight were carefully considered following [50,51].

Nominal strain was computed as $\delta(t)/L_0$ where L_0 is the initial sample height and validated using image-based tracking. Absorbed energy E_a was calculated up to the onset densification, defined as the strain corresponding to 1.3 times the plateau stress (average stress between strains 0.2–0.4) [52]. If densification was not reached, E_a was computed until the contact force returned to zero, indicating a rebound of the impactor, confirmed by high-speed camera footage. Specific energy absorption (SEA) was obtained by normalising E_a with specimen mass. The specimen's energy capacity is defined as the maximum energy absorbed through plastic deformation, irrespective of applied impact energy.

In addition to primary peak force (F_{max}), maximum displacement (δ_{max}), and impact duration (T), the Dynamic Increase Factor (DIF) was used to quantify strain rate sensitivity, defined as the ratio of dynamic to quasi-static yield stress ($\sigma_{y,d}/\sigma_{y,q}$). The dynamic yield stress ($\sigma_{y,d}$) was calculated as the first peak force divided by the nominal cross-sectional area (Eq. (2)). The dynamic modulus (E_d), or impact stiffness [53], was defined as the initial slope of the $\sigma - \delta$ curve within the $\delta = 0.015$–0.05 range. This interval was selected post-analysis for its consistent linearity below the yield point across all samples, allowing reliable quantification of elastic stiffness across different strain rates. To facilitate comparison with literature, mechanical properties were normalised by the corresponding bulk values of the base material (e.g. σ_s in Eq. (2)) from [54].

The effective dynamic modulus ($E_{d,tot}$) of the linearly graded lattices was estimated using a series-spring approximation, as defined in Eq. (3), following the approach described in [55,56]. The constants C and n were obtained by fitting to experimental data.

$$\overline{\sigma}_d = \frac{\sigma_d}{\sigma_s} = \frac{(F_{max}/A_{nominal})}{\sigma_s} \tag{2}$$

$$\frac{1}{\overline{E_{d,tot}}} = \frac{1}{L}\int_0^L \frac{1}{\overline{E_d(z)}}dz = \frac{1}{L}\int_0^L \frac{1}{C(\rho(z))^n}dz \tag{3}$$

2.4. Design of experiment

Table 3 and Table 4 summarise the testing matrix. In Table 3 examines the influence of lattice design parameters, including unit cell type and grading strategy under fixed conditions, while Table 4 explores the effects of varying impact energy and printing direction on selected lattice configurations. Each case was tested with a minimum of three repetitions to ensure consistency and reliability. Load–displacement curves are presented as average responses, while numerical properties (e.g. stiffness) are reported as mean ± standard deviation.

A uniform SP lattice with $\rho_{avg} = 0.5$ was selected as the benchmark for comparative analysis. In this context, 'parallel' and 'transverse' denote the alignment of the loading direction relative to the printing direction (Fig. 2). To facilitate comparison with previous literature,

Table 3
Testing matrix 1: varying design lattice approach while testing condition was fixed.

Testing conditions		Cell type	Material	Ungaded (**u**)			Graded (**g**)					
				ρ_{avg}			Density graded $\rho_{min} - \rho_{max}$			Cell size graded*		
PD	E_i[J]											
P	15	SP BCC*	Nylon / Onyx	0.2	0.35	0.5	0.4–0.6	0.3–0.7	0.2–0.8	3–4–5 –	3–5–7 –	3–6–9 –

* BCC lattice is not tested under cell size graded
Printing direction (PD): P/T – Parallel/Transverse, E_i – impact energy.

Table 4
Testing matrix 2: varying testing condition for chosen lattices.

Testing conditions		Cell type	Material	Ungraded (*u*)	Graded (*g*)	
				ρ_{avg}	Density graded $\rho_{min} - \rho_{max}$	Cell size graded
PD	E_i [J]					
P T	15 / 45 / 90 15	SP	Onyx	0.5	0.2–0.8	3–6–9

Printing direction (PD): P/T – Parallel/Transverse, E_i – impact energy.

mechanical properties are reported in normalised form relative to the bulk properties of the base material.

Sample codes were assigned systematically to identify each lattice configuration. The prefix (*SP* or *BCC*) denotes the UC topology, while the superscript (*u* or *g*) indicates whether the lattice is uniform or graded. The subscript specifies the grading range, as listed in Table 3. For instance, $BCC^{g}_{0.2-0.8}$ represents a BCC lattice with ρ graded from 0.2 to 0.8 and SP^{g}_{3-5-7} refer to SP lattice with cell size graded from 3 to 7 unit cells per edge length.

3. Experimental results

3.1. Materials properties

Onyx filament revealed a fibre volume fraction of 11.5 %, determined from a TGA fibre weight fraction of 13.51 %, along with carbon fibre density of 1.36 g/cm^3 and matrix density of 1.13 g/cm^3, as referenced in [41,42] (Fig. A, Appendix B). This fibre volume fraction consistent with the 9–12 % range reported in prior research [48,57,58]. Microscopic examination of a cryo-fractured Onyx filament confirmed a uniform distribution of short carbon fibres across the cross-sectional area (Fig. A-B, Appendix B). The near-circular fibre cross-sections, together with the shear alignment typically reported during extrusion [59] suggest a strong tendency for fibre orientation parallel to the extrusion direction [60]. In comparison to the intended density, the printed components exhibited a slightly lower relative density of ~4.29 % (Fig. A-C , Appendix B). This can be attributed to manufacturing factors such as print accuracy, porosity, and model discretisation.

3.2. Failure mechanism

Similar to typical quasi-static compressive behaviour [2], the dynamic behaviour of AM lattices can be divided into three stages: (i) an initial linear-elastic rise in force, (ii) a plastic deformation plateau, and (iii) a sharp force increase due to densification. It should be noted that Fig. 3 illustrates a representative force–displacement profile characteristic of quasi-static failure.

During the initial linear-elastic stage, Onyx lattices displayed partial elastic deformation (1.1, Fig. 3, allowing for some recovery post-deformation. Another deformation behaviour (1.2, Fig. 3) involved localised fracture, serving as precursors to catastrophic failure. These included shear banding (typically at ~45°) and crack propagation at stress concentration zones.

In the plateau region, two primary deformation mechanisms were observed. The first was layer-by-layer progressive collapse (2.1, Fig. 3), characterised by the sequential failure of individual unit cell layers, leading to multiple local peaks. The second was global compaction (2.2, Fig. 3), characterised by a continuous increase in force as the structure densified. Typically, the failure process involves a combination of these mechanisms, making the dominant mode hard to identify.

Post-impact, the impactor exhibited two primary movements: rebound and penetration. Rebound indicates partial recovery and incomplete failure, with a portion of the impact energy transforming back into potential energy. Consequently, energy absorption is calculated by subtracting rebound energy. Conversely, penetration occurs when the impactor embeds within the specimen, leading to energy dissipation predominantly through plastic deformation and densification. To ensure fair comparisons among specimens, final energy absorption metrics excluded contributions from densification processes.

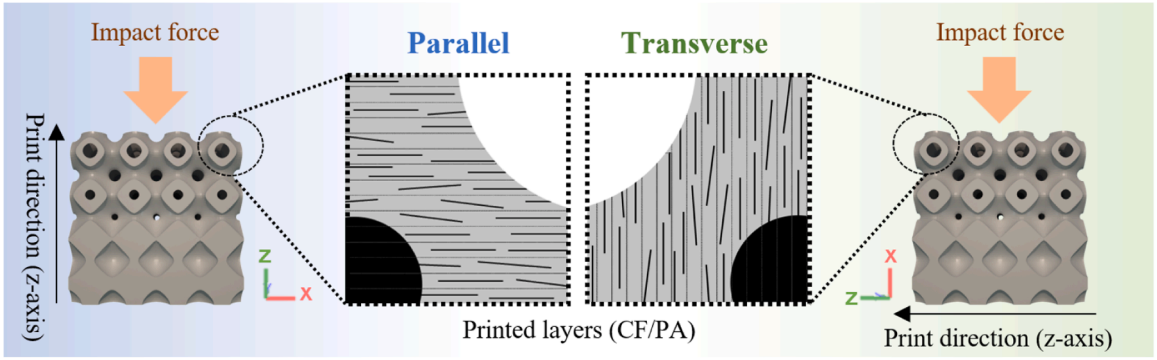


Fig. 2. Parallel and transverse printing direction.

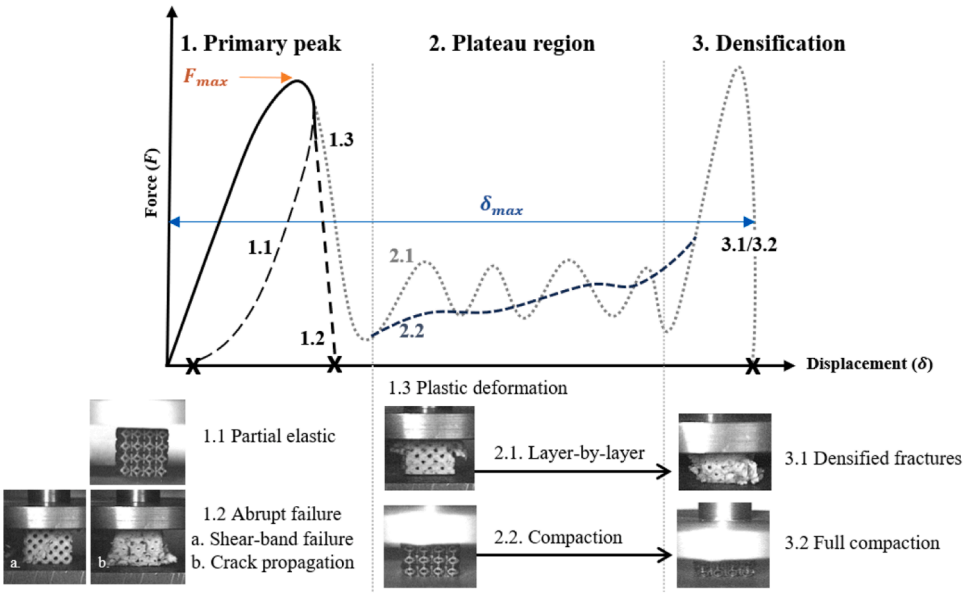


Fig. 3. Representative force–displacement response and corresponding deformation modes.

3.3. Force and energy profiles

Table 5 summarises the studied parameters and provides a structured basis for the experimental plots (Figs. 4–7) and the subsequent discussion. Several configurations, particularly graded lattices, exhibited dynamic behaviours that deviate from quasi-static trends, including additional failure mechanisms such as crack propagation. The results also reveal differences in impact energy absorption across configurations, which are less apparent in quasi-static or very high strain rate regimes.

The dynamic responses of all configurations are presented through the force–displacement and energy absorption curves. In the energy plots, densification onset is marked by a '◆', beyond which E_a is not assessed. The tested impact energies range from 15 to 90 J, correlating with strain rates of approximately 22 to 79 s^{-1}, consistent with the intermediate regime targeted in this investigation.

Overall, higher average relative densities ρ_{avg} and stretch-dominated SP lattices yield greater F_{max} and E_a. Grading significantly affects the deformation mechanism, often resulting in multiple peaks within the force response. Onyx specimens exhibiting more stable collapse modes and enhanced E_a compared to Nylon, particularly under higher impact energies.

4. Discussion

4.1. Effect of cell architecture and grading

4.1.1. Cell topology

The SP lattices outperformed the BCC lattices in both strength and stiffness (Fig. 4), consistent with previous quasi-static findings [6,61]. This is attributed to the stretching-dominated nature of the SP topology, which enables efficient load transfer through tension and compression across continuous surfaces [62,63]. In contrast, the bending-dominated BCC design exhibits lower axial load-bearing capacity, facilitating rapid geometric changes and crack initiation in its struts, often resulting in abrupt failure. High-speed imaging (Fig. 8) confirmed this observation. SP lattices displayed more distributed deformation, while BCC samples typically failed in a brittle manner, with fragments ejected near the interface between unit cell layers. This performance difference was consistent across ungraded configurations, with variation depending on design parameters. Given the consistence and more stable behaviour of SP lattices, they are used as the representative topology in the following discussion, except where BCC-specific trends are noted.

4.1.2. Relative density and grading

The widely adopted Gibson-Ashby power-law [4] was applied to the relative dynamic properties ($\overline{E_d}$, $\overline{\sigma_{y,d}}$), showing good agreement with experimental data ($R^2 > 0.98$). The fitted coefficients are summarised in Table 6. The fitted dynamic coefficients C_d were approximately twice those reported for the quasi-static regime C_q in [2,6], while the exponent values n_d remained comparable. This indicates that although the absolute stiffness and strength increase significantly under dynamic loading, the relative influence of ρ_{avg} remains of similar magnitude across both regimes. These results demonstrate that the power-law relationship remains valid under intermediate strain rates, regardless of topology or loading conditions.

In ungraded lattices, increasing ρ_{avg} led to more pronounced layer-

Table 5
Summary of studied parameters with corresponding figures and discussion references.

Parameters	Configuration of interest	Force and energy plots	Discussion Section	Key insight
Cell type	BCC, SP	Fig. 4	4.1.1	Consistent with QS
ρ	$\rho = 0.2, 0.35, 0.5$	Fig. 4	4.1.2	Consistent with QS; variation in mechanical properties observed
ρ grading	Uniform, Graded	Fig. 5	4.1.3	Consistent with QS; failure deviates under impact
Grading severity	3 severity levels	Fig. 5	4.1.2 / 4.1.3	Deviates from QS trend
Cell size grading	Uniform, Graded	Fig. 6	4.1.3	Deviates from QS trend
Fibre integration	Nylon, Onyx	Figs. 4–7	4.2.1	Distinct improvement in composite
Printing direction	Parallel, Transverse	Fig. 6	4.2.2	Mostly consistent with QS
Impact energy	$E_i = 15, 45, 90\ J$	Fig. 7	4.3.1	Distinct energy capacity for selected configurations
Strain rate	$\dot{\varepsilon} \approx 0.001 - 79\ s^{-1}$	Fig. 7	4.3.2	Rate sensitivity observed; analytical support provided

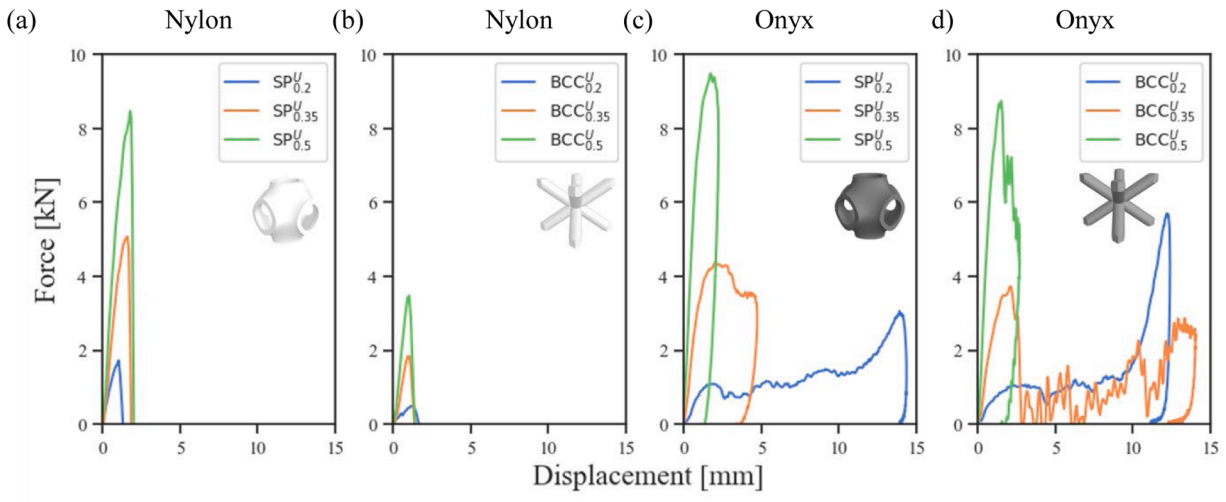


Fig. 4. Load–displacement curves for ungraded SP and BCC lattices ($\rho = 0.2, 0.35, 0.5$) The x-axis is limited to 15 mm for clarity (specimen height = 20 mm). White parts indicate Nylon specimens, while grey parts indicate Onyx.

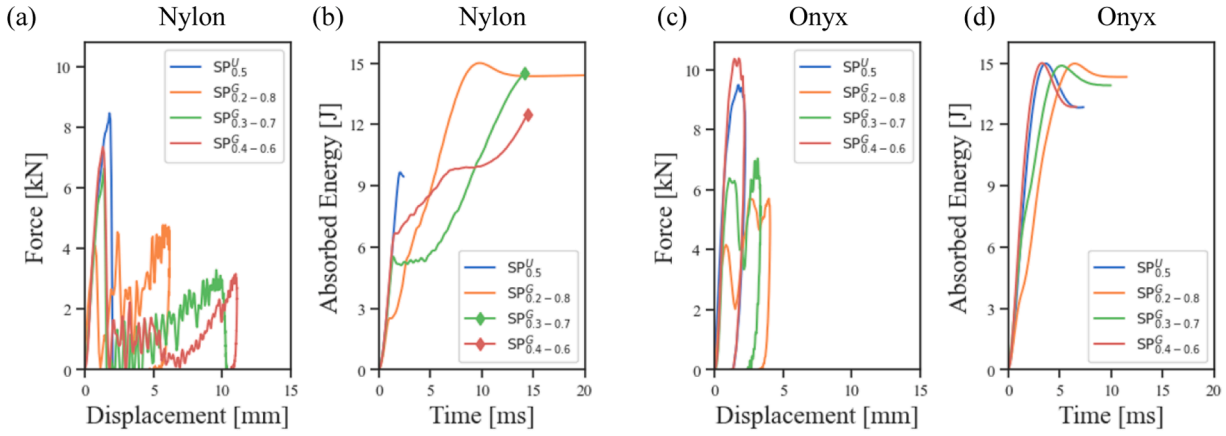


Fig. 5. Load–displacement curves and absorbed energy–time curves for relative density graded lattices.

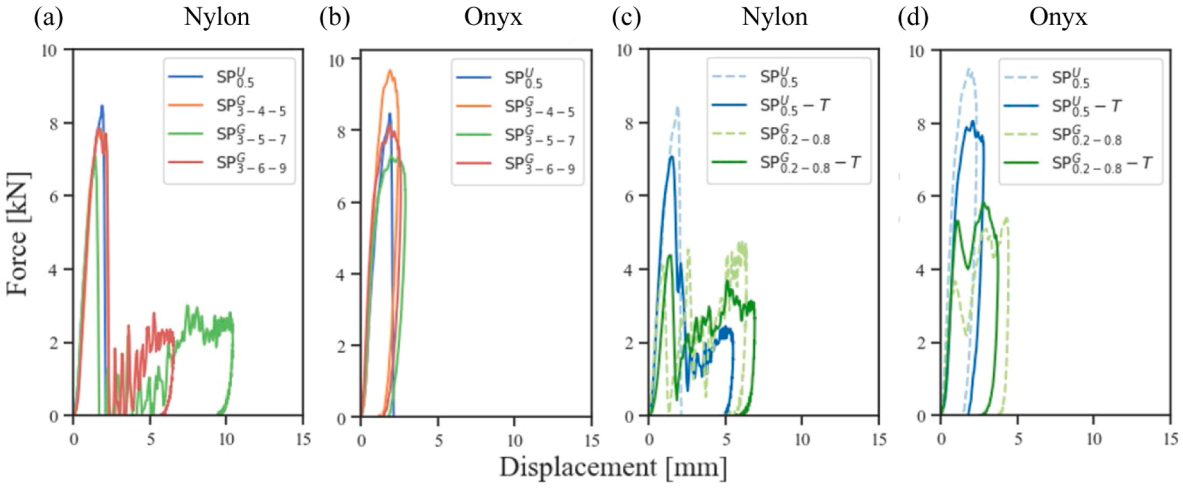


Fig. 6. Load-displacement curves illustrating (a–b) unit cell size–graded lattices and (c–d) printing direction effects (T refers to transverse).

by-layer failure, accompanied by a reduction in shear band formation. This shift in failure modes is in agreement with prior quasi-static findings for both BCC [64] and SP lattices [65], where increased local thickness enhances bending resistance and reduces the likelihood of global shear bands. In the case of BCC, this transition is accompanied by a reduction in bending-dominated behaviour. Under quasi-static loading, shear bands are commonly associated with global barrel-shaped deformation, a result of frictional constraints at the

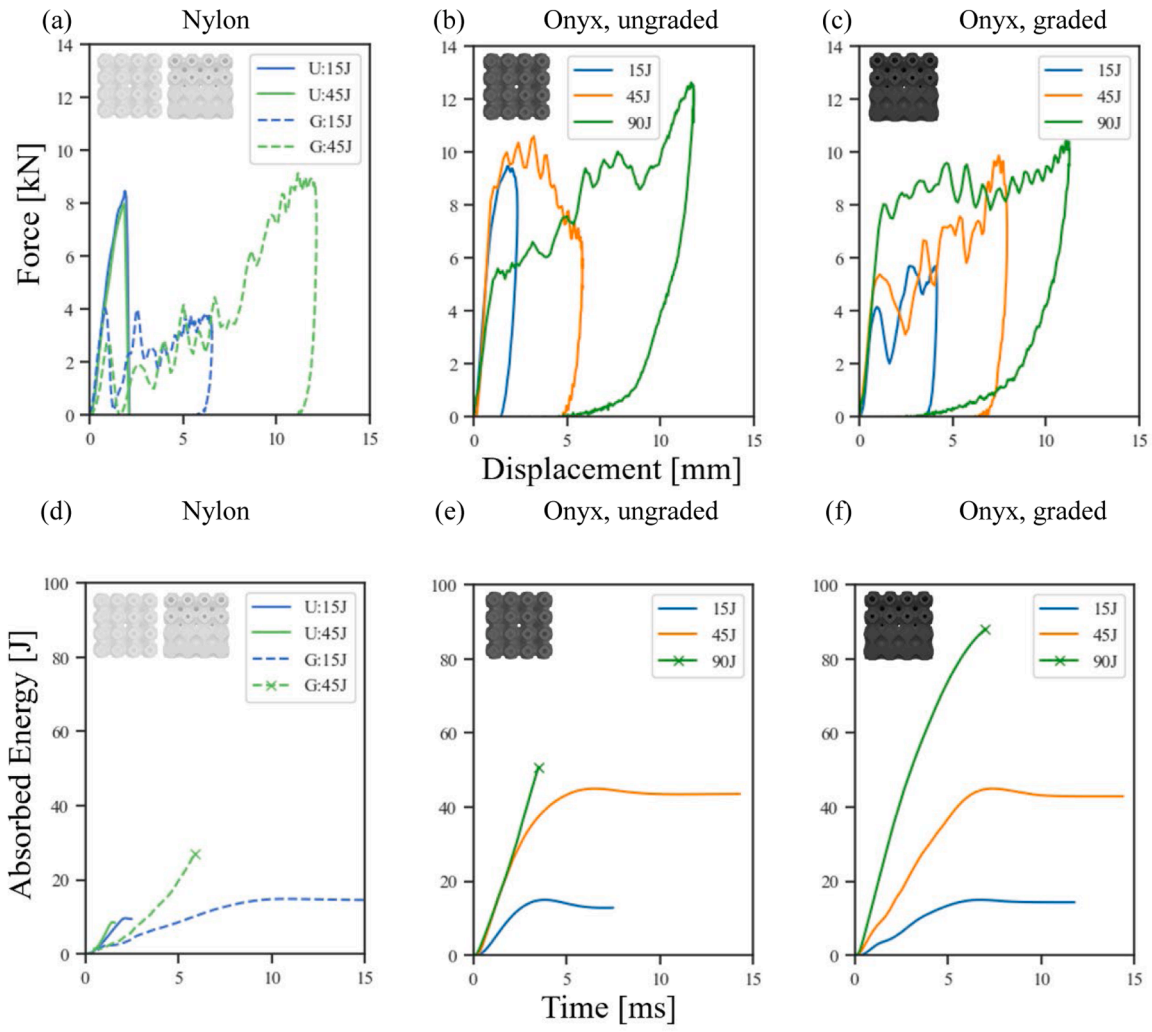


Fig. 7. (a–c) Load-displacement and (d–f) energy absorption curves for selected lattice configurations under varying impact energies (15–90 J).

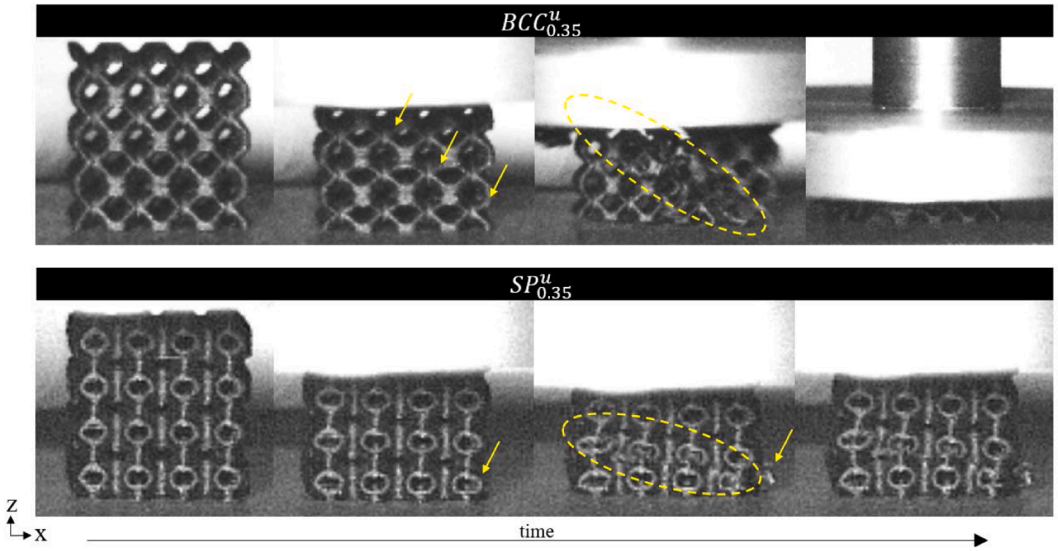


Fig. 8. BCC and SP ($\rho = 0.35$) Onyx lattices under impact event (15 J).

contact surfaces that limit lateral expansion [44,66]. However, such deformation was not observed under dynamic loading, likely due to the shorter timescale, which reduces the development of frictional constraint. Moreover, sudden fractures were more frequently observed in dynamic tests, suggesting that limited time for stress redistribution may promote brittle-like failure mechanisms compared to the more gradual failure under quasi-static conditions.

The density grading approach revealed a layer-by-layer failure mode

Table 6
Power-law coefficients from obtained dynamic properties (x_d).

Properties	Cell type	C_d	n_d	R_d^2
Relative modulus ($\overline{E}_d$)	SP	1.95	2.56	0.98
	BCC	2.46	3.15	0.99
Relative yield stress ($\overline{\sigma}_{y,d}$)	SP	2.36	2.02	0.98
	BCC	2.71	2.34	0.99

(Fig. 9b,d), distinct from the failure patterns observed in ungraded lattices, and led to straight-line cracks propagating parallel to the impact direction (from ρ_{min} to ρ_{max}, Fig. 9b). These cracks were not typically observed under quasi-static loading, likely due to slower deformation promoting more gradual failure rather than abrupt interfacial rupture. These failure mechanisms enhance crashworthiness, evidenced by the gradual increase of energy profile (Fig. 5c–d) and multiple peaks in force profiles (Fig. 5a–b). The multiple secondary peaks correspond to sequential layer failures until energy is fully dissipated, or densification occurs. Some secondary peaks showing a force drop to zero followed by recovery likely indicate complete fracture of the top layer and subsequent engagement of denser underlying regions. The initial peak of the F-δ curve is proportional to ρ_{min}, the region with the lowest E. Consequently, grading severity influences F_{max} and the secondary peaks, consistent with previous research under both quasi-static [5] and dynamic conditions [22,23]. The most severely graded lattices ($\Delta\rho = 0.2 - 0.8$) absorbed the highest energy surpassing both ungraded and moderately graded structures across all unit cell types. This contrasts with the quasi-static case, where severe grading in BCC lattices was found to be detrimental to performance.

Across the range of grading severity, the $\overline{E}_d$ of lattices was predicted using Eq. (3) and the coefficients in Table 6, with results shown in Fig. 10. The model predicted that the ungraded lattice would exhibit the highest stiffness. However, experimental data showed that the moderately graded SP lattice ($\Delta\rho = 0.4 - 0.6$) achieved the highest modulus. This discrepancy likely arises from the open-to-closed cell transition in SP unit cell as ρ exceeds 0.5, as reported in [6], which may not be fully captured by the fitted power-law model. Although all graded configurations involve this transition, the moderate case is more concentrated around it and thus more affected. In contrast, the severely graded lattice covers a broader range of ρ, reducing the influence of the transition and aligning better with predictions. For BCC lattices, which do not exhibit an open-to-closed transition, predictions matched experiments more consistently. However, greater scatter in BCC data, particularly for moderate grading, limits further interpretation. All $\overline{E}_d$ values exceeded their quasi-static baselines, confirming the influence of strain rate on lattice stiffness.

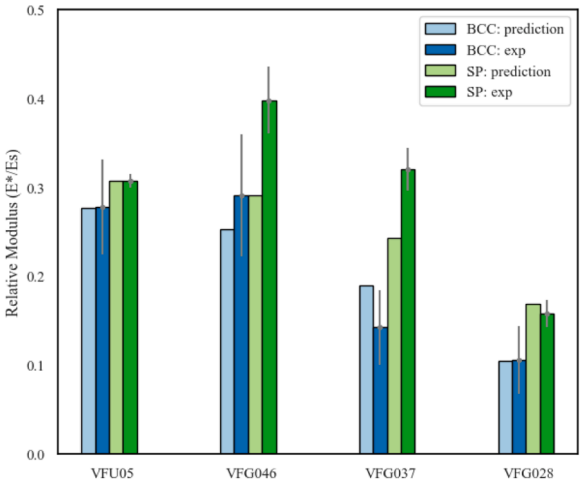


Fig. 10. Comparison between the predicted relative modulus ($\overline{E}$) of density-graded lattices and experimental results.

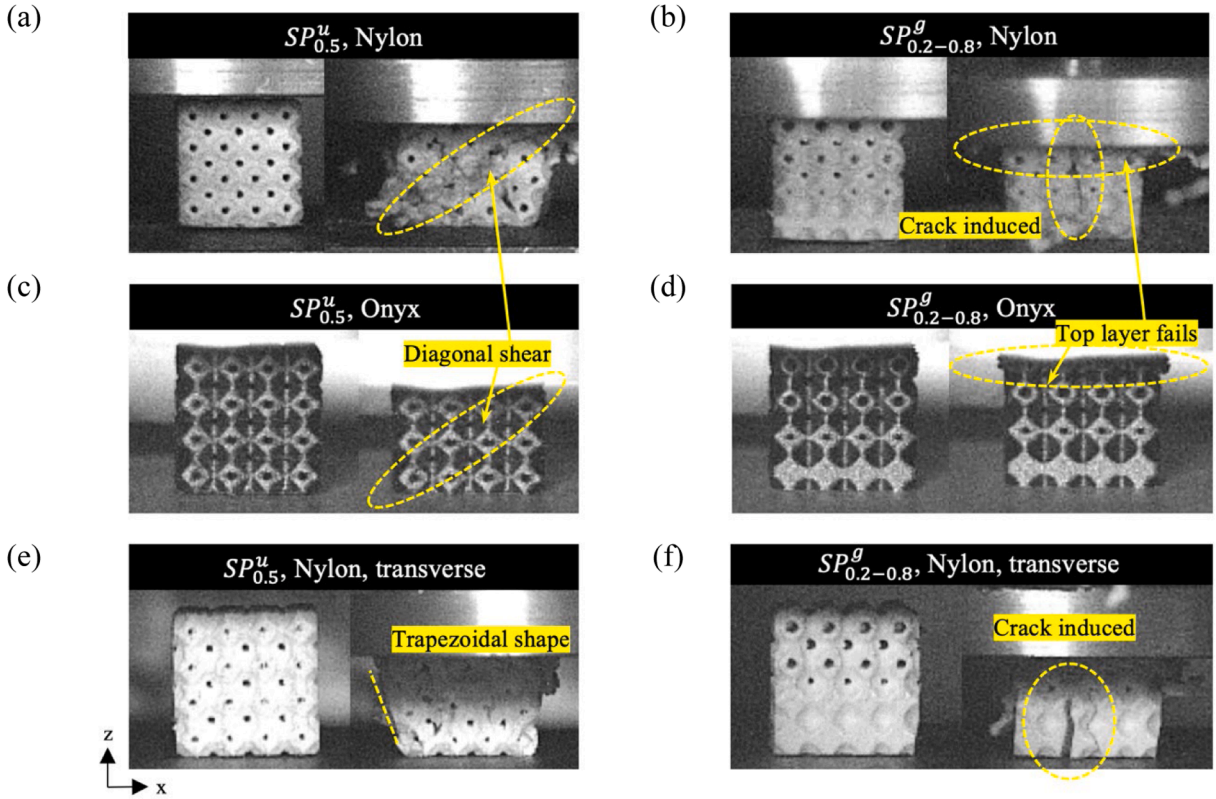


Fig. 9. Pre- and post-impact deformation of uniform and density-graded lattices under parallel and transverse loading directions (15 J Impact energy).

General conclusions can be drawn from the observed trends across levels of grading severity. Severely graded lattices were found to be better suited for high-energy absorption applications requiring large deformations (i.e., beyond densification) or multiple impacts. However, moderately graded lattices provided higher initial stiffness and reduced plastic deformation under low-energy impacts, offering advantages where contact stiffness and rebound control are desired. Therefore, the optimal grading strategy ultimately depends on the required impact scenario. These effects of grading severity were found to be largely independent of unit cell topology and base material, although the degree and mode of failure differed, as shown in Figs. 9a–d and 11a. High-speed imaging provided qualitative insight into failure modes, but limitations in resolution and lighting hindered detailed deformation analysis. Future studies could achieve quantitative assessment using 3D DIC with proper speckling, synchronised multi-cameras, and higher frame rates.

4.1.3. Cell size grading

Failure observations in cell-size graded lattices (Fig. 12) revealed both horizontal and vertical cracking, predominantly in the large-cell region, consistent with previous quasi-static findings [6,67]. However, under dynamic loading, failure process was more catastrophic, characterised by a sequential collapse and global crack propagation. Cracks initiated at stress concentrations near the mid-height of larger SP cells, where horizontal cracks coalesced along the XY plane, leading to unit cell-layer failure of the bottom region. This was typically followed by vertical or diagonal cracks, originating either from the neck regions between adjacent cells [68,69] or from mid-front surfaces, which propagated upward through the lattice and might deviated laterally around the denser upper layers, as shown in Fig. 12.

It could be deduced that within the unit cell size gradient, larger cells are more susceptible to failure than smaller ones. This behaviour may be attributed to two factors, assuming negligible shock wave effects. First, the lower tessellation in large-cell regions reduces geometric constraint, lowering local resistance to deformation [70,71]. Second, smaller-cell regions may experience over-deposition during printing, potentially increasing local stiffness and inhibit crack penetration.

As grading severity increases, global cracks increasingly diverge from straight-line propagation and take more diagonal paths, tending to bypass the smaller-cell top regions (Fig. 12). This behaviour is likely influenced by a combination of shear band formation [67], geometric confinement, and local stiffness contrast. Such deviation facilitates reduces failure near the impact surface, enabling continued load transfer and enhancing energy absorption. For example, SP^{g}_{3-6-9} demonstrated a 54.6 % increase in E_a (5.15 J), whereas SP^{g}_{3-4-5} performed comparably to the uniform benchmark.

For fibre-reinforced lattices, minimal variation in failure response was observed under low impact energy (15 J), with no clear trend in peak force across grading severities (Fig. 6b). Unlike the Nylon samples, no visible cracks or consistent deformation patterns were observed at this energy level, likely because the Onyx lattices had not yet reached global failure. The variation in F_{max} may be attributed to the morphing regions (illustrated in Fig. 1), which could affect local deformation behaviour, although their exact influence remains unclear. At 90 J, global cracks were observed to propagate from the larger to smaller cells (Fig. 11b), confirming that the influence of cell size grading extends across materials.

Although cell size grading had limited effect on peak force, it showed potential of improved energy absorption and enabled more controlled crack propagation under dynamic loading, distinguishing it from quasi-static behaviour where such benefits were less evident. These findings highlight a previously unreported mechanism by which size grading can manage failure progression, particularly in brittle materials where fine-cell regions help suppress surface fracture. As supported by post-impact observations (Fig. 11b), this grading strategy shows promise for protective skin design in sandwich structures and impact mitigation applications.

4.2. Material and printing effect

4.2.1. Fibre-reinforced composites

Post-impact examination revealed extensive surface cracking and brittle fracture in pure Nylon lattices, often resulting in fragmentation. In contrast, Onyx specimens exhibited more gradual deformation with minor local damage (Fig. 9). These differences may be stem from the presence of chopped carbon fibres, which are known to enhance toughness in composite [60]. Although fibre fracture or pull-out was not observed, the improved performance of Onyx suggests that fibre–matrix interactions, such as crack deflection or interfacial debonding, may contribute to the observed energy dissipation. These mechanisms are commonly reported in short-carbon fibre reinforced polymers [36] and may be active here despite the low fibre content. The present results therefore provide direct evidence, both through failure observations and energy absorption measurements, that fibre reinforcement can alter failure progression in AM lattices under dynamic loading, leading to more gradual deformation and reduced fragmentation compared with pure Nylon. Several studies [72,73] have reported ductile fracture in Onyx material, future in-situ microscopy or high-resolution imaging (e.g. SEM) could help verify these observations.

These trends are also reflected in the mechanical response. Onyx specimens showed smoother $F-\delta$ curves, while Nylon exhibited abrupt load drops Fig. 4). Quantitatively, Onyx absorbed 31.6 % more energy than the Nylon benchmark and dissipated >85 % of the applied 15 J, indicating improved damage tolerance. Onyx's energy profiles often peaked near δ_{max} and decreased during rebound, suggesting incomplete

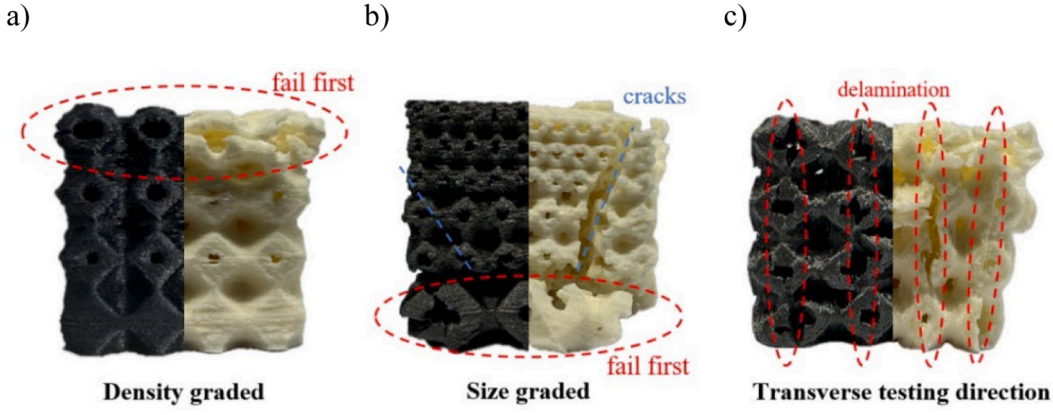


Fig. 11. Post-impact samples with cracks and failure region indicators: (a) Density-graded sample, (b) Size-graded sample, and (c) Sample tested in transverse direction.

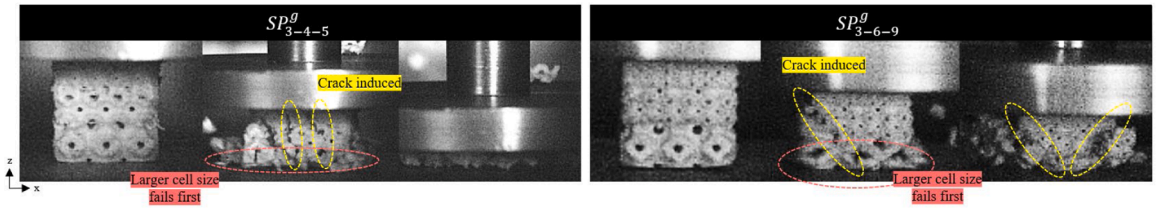


Fig. 12. Deformations of cell-size graded lattices (Nylon) under impact energy of 15 J.

failure and the potential for further energy absorption.

The influence of density grading was less pronounced in Onyx, with E_a improved by 8.4 % compared to 46.9 % in Nylon relative to their respective ungraded benchmarks. Additionally, the moderately graded Nylon reached the highest δ_{max}, while in Onyx, it was the most severely graded configuration (Fig. 5a). This difference may reflect how each material interacts with the density gradient. In Nylon, δ_{max} tends to rely on the denser base (ρ_{max}) to arrest failure progression, which occurs later in moderately graded configurations. In contrast, δ_{max} in Onyx is largely dominated by deformation in the low-density region (ρ_{min}), where most energy is dissipated without significant engagement of the denser sections.

Compared to other polymer-based lattices [74,75], the density-graded composite with 10 % CFVF demonstrates a high SEA, albeit at the cost of increased density (Fig. 13), indicating potential for high-impact energy absorption applications. According to the Halpin-Tsai model [76], increasing fibre volume fraction would raise both modulus and yield stress, assuming randomly fibre orientations. However, in the MEX process, achieving higher fibre content is limited by viscosity constraints, which affect printability and part quality (i.e., reduced porosity) [60]. Future advancements in AM may help overcome these limitations, enabling the production of stronger, lightweight composites for dynamic loading.

4.2.2. Influence of printing direction

Mechanical anisotropy is a typical feature in MEX-fabricated parts, where weaker interlayer bonding leads to delamination or buckling under transverse loading, while parallel loading tends to produce more uniform deformation [54]. This trend was confirmed experimentally, ungraded lattices exhibited directional sensitivity, with transverse loading causing reduced F_{max} and increased susceptibility to interlayer delamination and trapezoidal shape, as seen in post-impact specimens (Fig. 10c).

In contrast, density-graded lattices showed more consistent behaviour across printing directions. This improvement is likely due to enhanced structural homogeneity and stronger local bonding in high-density regions [6], which help mitigate delamination and local failure. Notably, graded Onyx lattices exhibited a 14.7 % increase in F_{max} under transverse loading. This may be attributed to partial fibre alignment along the print path in dense zones, as observed in microscopy [77] (Fig. B, Appendix B), which provides local reinforcement despite relatively low fibre volume fraction. These findings highlight the role of print strategy in impact performance and show that functionally graded designs can reduce printing directional sensitivity and promote more consistent responses.

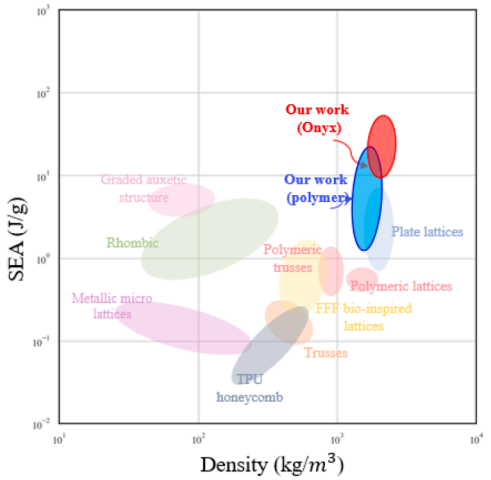


Fig. 13. SEA compared to polymer-based literatures (adapted from [74,75]).

4.3. Loading conditions

4.3.1. Impact energy response

The energy capacity of a lattice refers to the maximum energy it can absorb through plastic deformation, beyond which excess energy is dissipated through other mechanisms such as vibration, heat, or sound. Once this threshold is reached, capacity remains consistent regardless of increasing input energy. At higher impact energies (45 J and 90 J), the dominant failure mechanism remained consistent but became more severe, as expected under evaluated strain rates. Nylon specimens reached their energy capacity within a shorter time frame (Fig. 7d). Onyx specimens exhibited more localised failure modes (Fig. 14b, d) and reached greater δ_{max} (Fig. 7b,c), enabling them to accommodate the greater input energy.

Fig. 15a summarises the energy capacity across the tested impact energy range, highlighting the effect of grading and fibre reinforcement. Among the Nylon configurations, outperforming both the uniform and cell-size-graded designs (~14.7 J), in agreement with findings on thickness-graded honeycombs [23]. For Onyx, the density-graded lattice absorbed nearly all of the applied energy (97.8 % of 90 J), exceeding the uniform configuration (81.8 % of 90 J) (Fig. 15a). This enhancement is attributed to the combination of Onyx's ductility and the graded structure's ability to promote progressive deformation, leading to nearly three times energy absorption to Nylon.

While increasing impact energy results in greater applied momentum, peak force does not necessarily scale linearly. Material ductility, failure progression, and structural design all influence the force response. In graded Onyx, the peak force at 90 J exceeded that at 15 J (Fig. 7c), suggesting more effective load distribution through gradual engagement of denser regions. Conversely, the uniform Onyx showed a lower peak force at 90 J, likely due to early localised failure and full capacity utilisation (Fig. 7b). These results help define the threshold of lattice energy dissipation, enabling more predictive use of grading and fibre reinforcement to tailor impact performance and highlighting the crashworthiness potential of density-graded lattices. Further work is recommended to establish capacity limits across other lattice architectures and constituent materials.

4.3.2. Strain rate sensitivity

The Dynamic Increase Factor (DIF), representing the ratio of dynamic to quasi-static yield stress, was observed to increase with relative density (ρ_{avg}) across all tested lattices and materials. This trend is broadly consistent with previous studies on polymeric, ceramic, and metallic lattice systems [78–80], the magnitude of the increase varies.

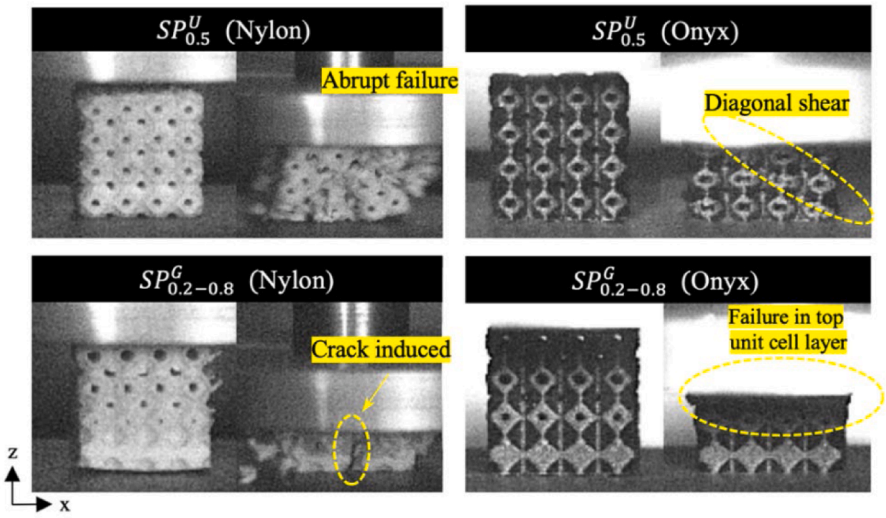


Fig. 14. Deformation of uniform and density-graded lattices under impact energy of 90 J.

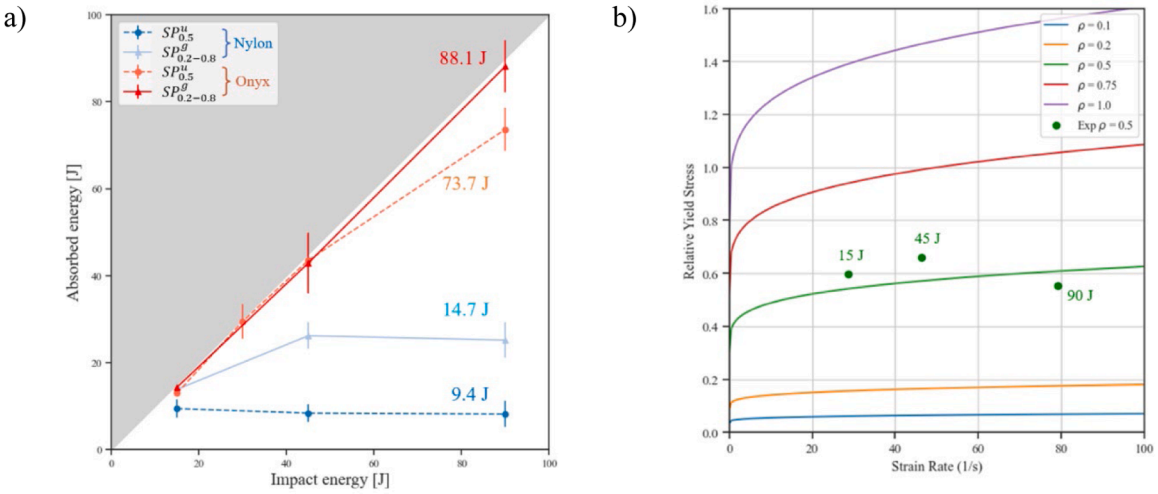


Fig. 15. (a) E_a for the ungraded and most severely density-graded lattices. The grey area indicates the unachievable region limited by applied impact energy. (b) $\overline{\sigma_d}$ vs $\dot{\varepsilon}$ for Onyx SP lattice at different ρ, derived using coefficients from Appendix C Experimental data for $\rho = 0.5$ under 15–90 J impacts are compared with the corresponding curve.

As the impact velocities in this study remain below the critical transition threshold [81] (Appendix C), inertial effects are considered negligible. Accordingly, the observed DIF trends are primarily governed by the constituent material and the lattice design.

In Table 7, it was observed that BCC lattices displayed a greater sensitivity to ρ_{avg} compared to SP architecture. This finding aligns with their higher power-law exponent n_d reported in Table 6 and follows the trend observed in quasi-static loading [4]. This is consistent with [80, 82], which indicated that bending-dominated lattices demonstrate increased strain-rate sensitivity due to greater strain localisation. However, this relationship does not generalise across all materials. For instance, in brittle ceramic lattices studied by Zhang et al. [78], designs with bending susceptibility exhibited reduced strain-rate sensitivity due to early fracture.

Onyx showed a steeper increase in DIF with ρ_{avg} compared to Nylon. This trend supported by findings by Ling et al. [79], who reported that ductile resin lattices exhibit pronounced strain-rate sensitivity, whereas brittle variants show minimal response. In unreinforced Nylon lattices, the strain-rate effect is governed by viscoelastic stiffening of the polymer matrix, where higher strain rates restrict molecular relaxation and

Table 7
DIFs values varied by the lattice topology and materials at $\dot{\varepsilon} \approx 22\ s^{-1}$.

	Onyx		Nylon	
ρ_{avg}	SP	BCC	SP	BCC
0.2	1.16±0.27	2.26±0.60	1.34±0.20	1.47±0.22
0.35	1.51±0.23	5.20±0.69	1.65±0.09	2.12±0.70
0.5	2.01±0.11	8.39±0.43	1.69±0.15	3.33±0.23

elevate apparent strength [83]. By contrast, composite lattices engage additional mechanisms, including fibre-induced constraint of deformation, suppressed matrix relaxation [84], and energy dissipation through the fibre–matrix interface and the fibres themselves. Collectively, these mechanisms amplify the dynamic response of reinforced lattices, yielding higher strain-rate sensitivity than in pure polymers, though the extent remains dependent on lattice topology. Further microscale studies are recommended to isolate and validate these effects, as alternative behaviours may arise in other multi-material systems. These findings emphasise the combined influence of fibre reinforcement and topology in governing rate-dependent behaviour.

$$\sigma_d = \sigma_y + \sigma_y\left(\frac{\dot{\varepsilon}}{a}\right)^{1/b} + \frac{\rho_0 v^2}{\varepsilon_d} \tag{4}$$

$$\sigma_d = \sigma_y\left(1 + \left(\frac{\dot{\varepsilon}}{a}\right)^{1/b}\right) \approx C(\rho)^n\left(1 + \left(\frac{\dot{\varepsilon}}{a}\right)^{1/b}\right) \tag{5}$$

Utilising the Cowper-Symonds (CS) model, Eq. (4) accounts for both strain rate and inertial effects in predicting dynamic yield stress. However, due to the relatively low impact velocities in this study, the inertial contribution (i.e., the third term in Eq. (4)) is negligible. This permits simplification to Eq. (5), which integrates the power-law relationship and ρ. The fitted coefficients (Appendix C), derived from quasi-static, 15 J, and 45 J data show high R^2 values, validating the model's suitability for both SP and BCC configurations.

The strain rate of Onyx SP lattices under 90 J reached a maximum of ~79.3 s^{-1} Fig. 15b presents the predicted σ_d of Onyx SP lattices as a function of $\dot{\varepsilon}$ and ρ. The high-impact experimental results align well with the $\rho = 0.5$ curve, confirming the model's validity. Extending the $\dot{\varepsilon}$ and ρ range in the future test would improve the model's predictive accuracy. The dynamic response is primarily governed by the intrinsic behaviour of the base material, arising from viscoelastic stiffening and strain hardening mechanisms within the polymer matrix [85–87]. Although quantifying the individual contributions requires molecular-scale analysis, their influence is evident in the observed lattice behaviour.

To isolate material effects from architectural influences, bulk Nylon and Onyx specimens (100 % infill) were tested across interested strain rates (fitted coefficients in Appendix C). As shown in Fig. 16, Onyx exhibited greater sensitivity to increasing strain rate, consistent with the quasi-static results [46]. The $\overline{\sigma}_d$ of the stretch-dominated SP lattice exceeded that of the corresponding bulk and BCC configurations. The trends between lattice types and materials diverged across strain rate, reflecting clear differences in the strain rate sensitivity. This confirms that dynamic behaviour is governed not only by the constituent material, but also by the influence of lattice architecture.

5. Conclusion

This study systematically investigated the dynamic behaviour of composite AM lattice structures under intermediate strain rate conditions using drop-weight impact testing. By concurrently evaluating multiple design and loading parameters, it offers a comprehensive understanding of their interplay and provides valuable insight for crashworthiness applications. The main findings are summarised below:

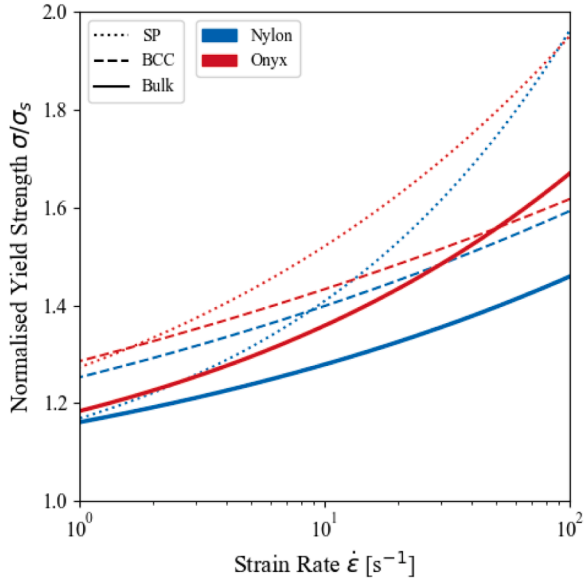


Fig. 16. Comparison of normalised dynamic strength $\overline{\sigma}_d$ as a function of strain rate ($\dot{\varepsilon}$) between lattice structures and their corresponding base materials.

5.1. Stretching- vs bending behaviour

- The stretching-dominated SP lattice outperforms the bending-dominated BCC lattice in both yield stress and energy absorption, regardless of relative density, constituent material, or grading strategy.
- Each lattice retained its characteristic failure mode across strain rates, with BCC lattices showed greater sensitivity to dynamic loading.

5.2. Grading strategies

- Density grading enhanced energy absorption through progressive, layer-wise deformation. The most severe grading achieved the highest energy absorption, while a moderately graded SP lattice unexpectedly showed the highest modulus.
- Failure tended to initiate in regions with larger cell size or lower density. Fractures subsequently propagated along the loading direction, from the initial failure to the opposite surface.

5.3. Comparison with quasi-static and plasticity model

- Failure mechanisms observed under dynamic loading resembled quasi-static trends with more pronounced damage. The influence of relative density remained apparent, with varying degrees depending on cell type and material.
- Experimental results aligned well with the Cowper–Symonds model, with quasi-static yield stress serving as the primary governing factor.

5.4. Constituent and printing direction

- Carbon fibres enhanced energy absorption by promoting ductility. Despite the low fibre volume fraction, Onyx exhibited partial elastic recovery, while Nylon underwent catastrophic fracture.
- The inclusion of fibres increased strain-rate sensitivity by engaging additional mechanisms beyond matrix viscoelasticity, with the extent of this effect remaining geometry-dependent.
- Transverse printing reduced peak force in ungraded lattices, likely due to weaker interlayer bonds. However, graded parts achieved comparable peak forces and more stable deformation, benefiting from increased homogeneity in high-density regions.

Future studies could incorporate stretch-dominated truss-based lattices, such as the Octet structure, to bridge truss- and surface-based architectures. Expanding the strain rate range is recommended to better capture dynamic behaviour and improve the accuracy of fitted coefficients. Further investigations that provide deeper insights are encouraged to supplement experimental work through the finite element analysis. As this study was limited by a fixed and low CFVF due to the use of commercial feedstock, alternative fabrication techniques could be explored to enable higher fibre content. Additionally, investigating hierarchical architectures and multi-material AM may further enhance multifunctionality and tailored impact performance.

CRediT authorship contribution statement

Piyapat Jameekornkul: Writing – review & editing, Writing – original draft, Methodology, Investigation, Formal analysis, Data curation, Conceptualization. **Ajit Panesar:** Writing – review & editing, Supervision, Methodology, Investigation, Formal analysis, Conceptualization.

Declaration of competing interest

The authors declare that they have no known competing financial interests or personal relationships that could have appeared to influence the work reported in this paper.

Appendix A

Table A

Table A
Summarises the parameters studied for the dynamic behaviour of AM lattices (2019–2024).

Studies	UC type	Modified / Hybrid	Relative density / Cell size	Stretching vs bending	Print / loading orientation	Composite	Graded	Dynamic behaviour
[1–6]	✓		✓					✓
[7–14]		✓						✓
[15–21]	✓		[20]	✓				✓
[22–24]					✓			✓
[25–27]	✓					✓		✓
[28–35]							✓	✓
[]	✓	[37]		✓		✓		✓
[38]*	✓		✓	✓	✓	✓	✓	

* Our group's earlier work on quasi-static compressive behaviour.

[1] Uddin M.A. et al., Sci. Rep., 2025. doi: 10.1038/s41598–024–84507–9.
[2] Coluccia A. et al., Mech. Adv. Mater. Struct., 2023. doi: 10.1080/15376494.2022.2064016.
[3] Maconachie T. et al., Int. J. Adv. Manuf. Technol., 2022. doi: 10.1007/s00170–021–08203-y.
[4] Duan Y. et al., Int. J. Impact Eng., 2019. doi: 10.1016/j.ijimpeng.2019.05.017.
[5] Zhou H. et al., Int. J. Mech. Sci., 2020. doi: 10.1016/j.ijmecsci.2020.105480.
[6] AlMahri S. et al., Addit. Manuf., 2021. doi: 10.1016/j.addma.2021.102220.
[7] Cao X. et al., Thin-Walled Struct., 2020. doi: 10.1016/j.tws.2019.106586.
[8] Li S. et al., Thin-Walled Struct., 2020. doi: 10.1016/j.tws.2020.107153.
[9] Li X. et al., Addit. Manuf., 2021. doi: 10.1016/j.addma.2021.102054.
[10] Song W. et al., Int. J. Impact Eng., 2023. doi: 10.1016/j.ijimpeng.2023.104752.
[11] Zhang X. et al., J. Eur. Ceram. Soc., 2022. doi: 10.1016/j.jeurceramsoc.2022.08.018.
[12] Xiao L. et al., Int. J. Impact Eng., 2022. doi: 10.1016/j.ijimpeng.2022.104333.
[13] Wang X. et al., Thin-Walled Struct., 2023. doi: 10.1016/j.tws.2022.110434.
[14] Ramos H. et al., Addit. Manuf., 2023. doi: 10.1016/j.addma.2023.103751.
[15] Bernard A.R. et al., Materials, 2024. doi: 10.3390/ma17071597.
[16] Weeks J.S. et al., J. Dyn. Behav. Mater., 2023. doi: 10.1007/s40870–022–00359–2.
[17] Hazeli K. et al., Mater. Des., 2019. doi: 10.1016/j.matdes.2019.107826.
[18] Jin N. et al., J. Dyn. Behav. Mater., 2022. doi: 10.1007/s40870–021–00318–3.
[19] Jin N. et al., Mater. Des., 2019. doi: 10.1016/j.matdes.2019.107655.
[20] Al-Ketan O. et al., J. Mater. Res., 2018. doi: 10.1557/jmr.2018.1.
[21] Fang Z. et al., Compos. Struct., 2021. doi: 10.1016/j.compstruct.2021.114414.
[22] Barnes B. et al., Addit. Manuf., 2021. doi: 10.1016/j.addma.2021.102466.
[23] Yu B. et al., Compos. Struct., 2021. doi: 10.1016/j.compstruct.2020.113500.
[24] Logakannan K.P. et al., Mech. Mater., 2020. doi: 10.1016/j.mechmat.2020.103503.
[25] Hou W. et al., Int. J. Mech. Sci., 2023. doi: 10.1016/j.ijmecsci.2023.108198.
[26] Kreide C. et al., Prog. Addit. Manuf., 2024. doi: 10.1007/s40964–023–00529–1.
[27] Wang J. et al., Thin-Walled Struct., 2022. doi: 10.1016/j.tws.2021.108810.
[28] Andrew J.J. et al., Int. J. Impact Eng., 2019. doi: 10.1016/j.ijimpeng.2019.103360.
[29] Santiago R. et al., Int. J. Impact Eng., 2023. doi: 10.1016/j.ijimpeng.2023.104592.
[30] Xiao L., Song W., Int. J. Impact Eng., 2018. doi: 10.1016/j.ijimpeng.2017.09.018.
[31] Sienkiewicz J. et al., Metals, 2020. doi: 10.3390/met10020213.
[32] Rodrigo C. et al., Eng. Struct., 2023. doi: 10.1016/j.engstruct.2023.115909.
[33] Feng G. et al., Int. J. Impact Eng., 2023. doi: 10.1016/j.ijimpeng.2023.104554.
[34] Xiao L. et al., Thin-Walled Struct., 2020. doi: 10.1016/j.tws.2020.106970.
[35] Zhang M. et al., Compos. Struct., 2023. doi: 10.1016/j.compstruct.2022.116405.
[36] Zhou J. et al., Int. J. Mech. Sci., 2023. doi: 10.1016/j.ijmecsci.2022.108054.
[37] Andrew J.J. et al., Mater. Des., 2021. doi: 10.1016/j.matdes.2021.109516.
[38] Plocher J., Panesar A., Addit. Manuf., 2020. doi: 10.1016/j.addma.2020.101171.

Appendix B

Fig. A

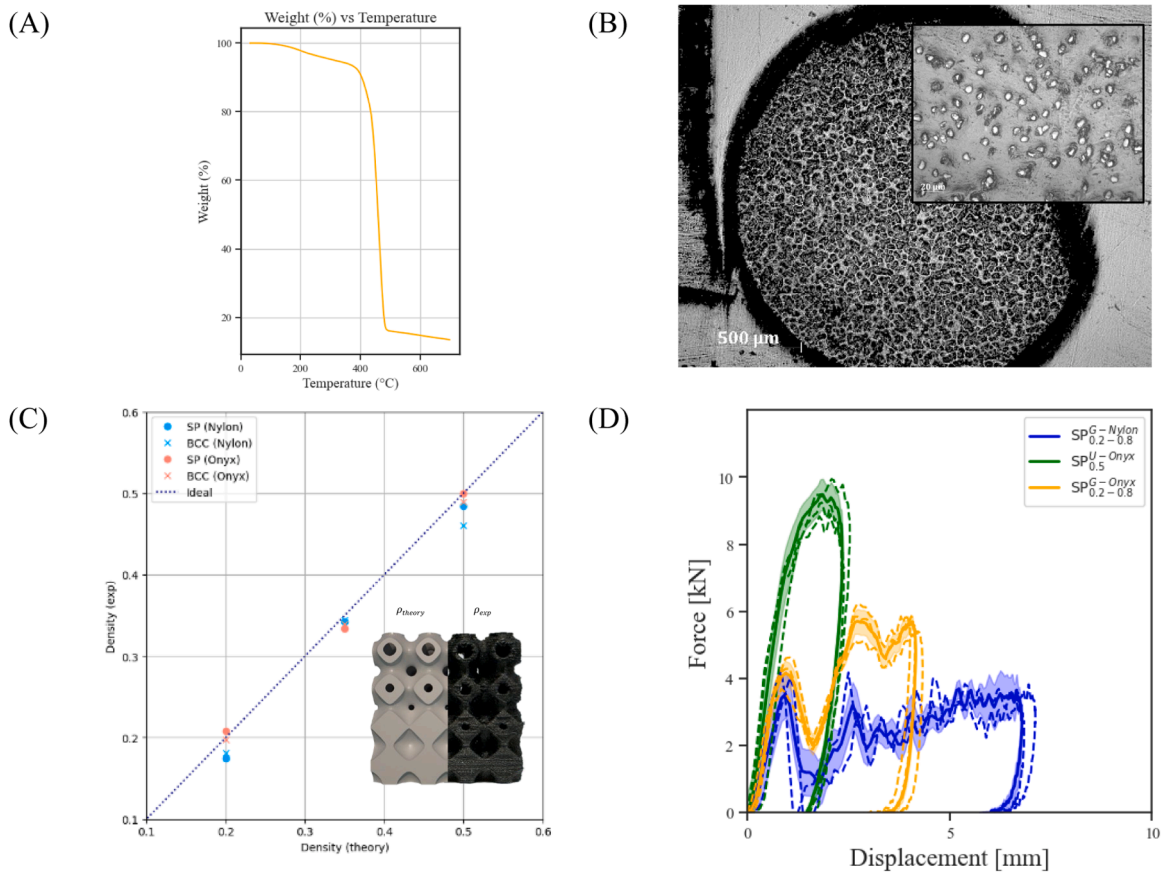


Fig. (A). (A) TGA results indicating Onyx's weight fraction; (B) Microscopy image showing the cross-sectional area of the Onyx filament; (C) Comparison between as built and theoretical density; (D) Force-displacement plots of selected lattices with SD illustrating the repeatability.

Appendix C

The critical impact velocity u_{cr} represents the threshold above which dynamic deformation transitions from strain rate–dominated to inertia- or wave-dominated behaviour. It is estimated based on the material's capacity to elastically deform prior to significant inertial effects [81]. This is expressed as

$$u_{cr} = \varepsilon_y c_e = \frac{\sigma_y}{E}\sqrt{\frac{E}{\rho}} = \frac{\sigma_y}{\sqrt{E\rho}}$$

where ε_y is the quasi-static yield strain and ρ is the material density. Using compressive properties from [54], the calculated critical velocities for Onyx and Nylon are as follows:

The critical velocity coresponding to given bulk material properties.

Material	σ_y [MPa]	E [GPa]	$\rho_{bulk}\left[\frac{kg}{m^3}\right]$	u_{cr} [m /s]
Onyx	39.81	1.383	1180	31.2
Nylon	41.65	1.089	1100	38.0

The table below presents the fitted coefficients for the lattices and bulk materials based on the Cowper–Symonds model (Eq. (4)). These values are plotted in Fig. 16, which highlight divergent behaviours between different lattice types and the bulk material.

Coefficients and corresponding errors of Eq. (4) derived from fitting experimental results.

	a		b		R^2	
	Nylon	Onyx	Nylon	Onyx	Nylon	Onyx
SP	102.63	71.02	2.76	4.19	0.98	0.92
BCC	144.39	6.83	8.03	10.24	0.94	0.97
Bulk	2429.02	336.08	5.46	3.99	0.91	0.92

Data availability

Data will be made available on request.

References

[1] Yin H, Zhang W, Zhu L, Meng F, Liu J, Wen G. Review on lattice structures for energy absorption properties. Compos Struct Jan. 2023;304:116397. https://doi.org/10.1016/j.compstruct.2022.116397.

[2] Maconachie T, et al. SLM lattice structures: properties, performance, applications and challenges. Mater Des Dec. 2019;183:108137. https://doi.org/10.1016/j.matdes.2019.108137.

[3] Alketan O, Rowshan R, Al-Rub RAbu. Topology-mechanical property relationship of 3D printed strut, skeletal, and sheet based periodic metallic cellular materials. Addit Manuf Jan. 2018;19:167–83. https://doi.org/10.1016/j.addma.2017.12.006.

[4] Gibson LJ, Ashby MF. Cellular solids: structure and properties. Cambridge solid state science series. 2nd ed. Cambridge: Cambridge University Press; 1997. https://doi.org/10.1017/CBO9781139878326.

[5] Rahman O, Uddin KZ, Muthulingam J, Youssef G, Shen C, Koohbor B. Density-graded cellular solids: mechanics, fabrication, and applications. Adv Eng Mater 2022;24(1). https://doi.org/10.1002/adem.202100646. Art. no. 1.

[6] Plocher J, Panesar A. Effect of density and unit cell size grading on the stiffness and energy absorption of short fibre-reinforced functionally graded lattice structures. Addit Manuf May 2020;33:101171. https://doi.org/10.1016/j.addma.2020.101171.

[7] Yang N, Quan Z, Zhang D, Tian Y. Multi-morphology transition hybridization CAD design of minimal surface porous structures for use in tissue engineering. Comput-Aided Des Nov. 2014;56:11–21. https://doi.org/10.1016/j.cad.2014.06.006.

[8] Li Y, et al. A review on functionally graded materials and structures via additive manufacturing: from multi-scale design to versatile functional properties. Adv Mater Technol 2020;5(6):1900981. https://doi.org/10.1002/admt.201900981.

[9] Raj R, Jiyalal Prajapati M, Tsai J-T, Kumar A, Jeng J-Y. Design and additive manufacturing of novel hybrid lattice metamaterial for enhanced energy absorption and structural stability. Mater Des Sept. 2024;245:113268. https://doi.org/10.1016/j.matdes.2024.113268.

[10] He M, et al. Compressive performance and fracture mechanism of bio-inspired heterogeneous glass sponge lattice structures manufactured by selective laser melting. Mater Des Feb. 2022;214:110396. https://doi.org/10.1016/j.matdes.2022.110396.

[11] Nian Y, Wan S, Wang X, Zhou P, Avcar M, Li M. Study on crashworthiness of nature-inspired functionally graded lattice metamaterials for bridge pier protection against ship collision. Eng Struct Feb. 2023;277:115404. https://doi.org/10.1016/j.engstruct.2022.115404.

[12] Álvarez-Trejo A, Cuan-Urquizo E, Bhate D, Roman-Flores A. Mechanical metamaterials with topologies based on curved elements: an overview of design, additive manufacturing and mechanical properties. Mater Des Sept. 2023;233:112190. https://doi.org/10.1016/j.matdes.2023.112190.

[13] Ha NS, Lu G. A review of recent research on bio-inspired structures and materials for energy absorption applications. Compos Part B Eng Jan. 2020;181:107496. https://doi.org/10.1016/j.compositesb.2019.107496.

[14] Meza LR, Zelhofer AJ, Clarke N, Mateos AJ, Kochmann DM, Greer JR. Resilient 3D hierarchical architected metamaterials. Proc Natl Acad Sci Sept. 2015;112(37):11502–7. https://doi.org/10.1073/pnas.1509120112.

[15] Daynes S. High stiffness topology optimised lattice structures with increased toughness by porosity constraints. Mater Des Aug. 2023;232:112183. https://doi.org/10.1016/j.matdes.2023.112183.

[16] Medvedev AE, Maconachie T, Leary M, Qian M, Brandt M. Perspectives on additive manufacturing for dynamic impact applications. Mater Des Sept. 2022;221:110963. https://doi.org/10.1016/j.matdes.2022.110963.

[17] Bois PDu, Chou C, Fileta B, Khalil T. Vehicle crashworthiness and occupant protection. Michigan: American Iron and Steel Institute; 2004.

[18] Shim J, Mohr D. Using split Hopkinson pressure bars to perform large strain compression tests on polyurea at low, intermediate and high strain rates. Int J Impact Eng Sept. 2009;36(9):1116–27. https://doi.org/10.1016/j.ijimpeng.2008.12.010.

[19] Arslan Bin Riaz M, Güden M. A review of the experimental and numerical studies on the compression behavior of the additively produced metallic lattice structures at high and low strain rates. Def Technol Jan. 2025. https://doi.org/10.1016/j.dt.2025.01.003.

[20] Li X, Xiao L, Song W. Compressive behavior of selective laser melting printed gyroid structures under dynamic loading. Addit Manuf Oct. 2021;46:102054. https://doi.org/10.1016/j.addma.2021.102054.

[21] Uddin MA, Andrew JJ, Barsoum I, Kumar S, Schiffer A. Quasi-static and dynamic compression behavior of stacked pyramidal lattice structures with I-beam struts. Sci Rep Jan. 2025;15(1):2837. https://doi.org/10.1038/s41598-024-84507-9.

[22] Rodrigo C, Xu S, Durandet Y, Fraser D, Ruan D. Quasi-static and dynamic compression of additively manufactured functionally graded lattices: experiments and simulations. Eng Struct June 2023;284:115909. https://doi.org/10.1016/j.engstruct.2023.115909.

[23] Andrew JJ, Ubaid J, Hafeez F, Schiffer A, Kumar S. Impact performance enhancement of honeycombs through additive manufacturing-enabled geometrical tailoring. Int J Impact Eng Dec. 2019;134:103360. https://doi.org/10.1016/j.ijimpeng.2019.103360.

[24] Dwyer CM, et al. Impact performance of 3D printed spatially varying elastomeric lattices. Polymers (Basel) Jan. 2023;15(5). https://doi.org/10.3390/polym15051178. Art. no. 5.

[25] Feng G, Li S, Xiao L, Song W. Mechanical properties and deformation behavior of functionally graded TPMS structures under static and dynamic loading. Int J Impact Eng Apr. 2023;176:104554. https://doi.org/10.1016/j.ijimpeng.2023.104554.

[26] Harris JA, Winter RE, McShane GJ. Impact response of additively manufactured metallic hybrid lattice materials. Int J Impact Eng June 2017;104:177–91. https://doi.org/10.1016/j.ijimpeng.2017.02.007.

[27] Li X, Xiao L, Song W. Compressive behavior of selective laser melting printed gyroid structures under dynamic loading. Addit Manuf Oct. 2021;46:102054. https://doi.org/10.1016/j.addma.2021.102054.

[28] Tancogne-Dejean T, Spierings AB, Mohr D. Additively-manufactured metallic micro-lattice materials for high specific energy absorption under static and dynamic loading. Acta Mater Sept. 2016;116:14–28. https://doi.org/10.1016/j.actamat.2016.05.054.

[29] Tancogne-Dejean T, Li X, Diamantopoulou M, Roth CC, Mohr D. High strain rate response of additively-manufactured plate-lattices: experiments and modeling. J Dyn Behav Mater Sept. 2019;5(3):361–75. https://doi.org/10.1007/s40870-019-00219-6.

[30] Quan C, Han B, Hou Z, Zhang Q, Tian X, Lu TJ. 3d printed continuous fiber reinforced composite auxetic honeycomb structures. Compos Part B Eng Apr. 2020;187:107858. https://doi.org/10.1016/j.compositesb.2020.107858.

[31] Zhou J, Liu H, Dear JP, Falzon BG, Kazancı Z. Comparison of different quasi-static loading conditions of additively manufactured composite hexagonal and auxetic cellular structures. Int J Mech Sci Apr. 2023;244:108054. https://doi.org/10.1016/j.ijmecsci.2022.108054.

[32] Andrew JJ, Verma P, Kumar S. Impact behavior of nanoengineered, 3D printed plate-lattices. Mater Des Apr. 2021;202:109516. https://doi.org/10.1016/j.matdes.2021.109516.

[33] Andrew JJ, Alhashmi H, Schiffer A, Kumar S, Deshpande VS. Energy absorption and self-sensing performance of 3D printed CF/PEEK cellular composites. Mater Des Oct. 2021;208:109863. https://doi.org/10.1016/j.matdes.2021.109863.

[34] Caminero MA, García-Moreno I, Rodríguez GP, Chacón JM. Internal damage evaluation of composite structures using phased array ultrasonic technique: impact damage assessment in CFRP and 3D printed reinforced composites. Compos Part B Eng May 2019;165:131–42. https://doi.org/10.1016/j.compositesb.2018.11.091.

[35] Hunt CJ, Morabito F, Grace C, Zhao Y, Woods BKS. A review of composite lattice structures. Compos Struct Mar. 2022;284:115120. https://doi.org/10.1016/j.compstruct.2021.115120.

[36] Aghajani S, Wu C, Li Q, Fang J. Additively manufactured composite lattices: a state-of-the-art review on fabrications, architectures, constituent materials, mechanical properties, and future directions. Thin-Walled Struct Apr. 2024;197:111539. https://doi.org/10.1016/j.tws.2023.111539.

[37] Coluccia A, Jiang Gianni, Meyer Guillaume, De Pasquale Giorgio, Mittelstedt C. Nonlinear static and dynamic modeling of energy absorption lattice structures behavior. Mech Adv Mater Struct July 2023;30(14):2838–49. https://doi.org/10.1080/15376494.2022.2064016.

[38] Duan Y, Du B, Shi X, Hou B, Li Y. Quasi-static and dynamic compressive properties and deformation mechanisms of 3D printed polymeric cellular structures with Kelvin cells. Int J Impact Eng Oct. 2019;132:103303. https://doi.org/10.1016/j.ijimpeng.2019.05.017.

[39] Zhou J, Liu H, Dear JP, Falzon BG, Kazancı Z. Comparison of different quasi-static loading conditions of additively manufactured composite hexagonal and auxetic cellular structures. Int J Mech Sci Apr. 2023;244:108054. https://doi.org/10.1016/j.ijmecsci.2022.108054.

[40] Aremu AO, et al. A voxel-based method of constructing and skinning conformal and functionally graded lattice structures suitable for additive manufacturing. Addit Manuf Jan. 2017;13:1–13. https://doi.org/10.1016/j.addma.2016.10.006.
[41] Panesar A, Abdi M, Hickman D, Ashcroft I. Strategies for functionally graded lattice structures derived using topology optimisation for Additive manufacturing. Addit Manuf Jan. 2018;19:81–94. https://doi.org/10.1016/j.addma.2017.11.008.
[42] Calladine CR. Buckminster Fuller's 'Tensegrity' structures and Clerk Maxwell's rules for the construction of stiff frames. Int J Solids Struct Jan. 1978;14(2): 161–72. https://doi.org/10.1016/0020-7683(78)90052-5.
[43] Ghaemi Khiavi S, Sadeghi BMohammad, Divandari M. Effect of topology on strength and energy absorption of PA12 non-auxetic strut-based lattice structures. J Mater Res Technol Nov. 2022;21:1595–613. https://doi.org/10.1016/j.jmrt.2022.09.116.
[44] Al-Ketan O, Lee D-W, Rowshan R, Abu Al-Rub RK. Functionally graded and multi-morphology sheet TPMS lattices: design, manufacturing, and mechanical properties. J Mech Behav Biomed Mater Feb. 2020;102:103520. https://doi.org/10.1016/j.jmbbm.2019.103520.
[45] "Carbon Fiber composite 3D printer: markforged Mark two." Accessed: June 11, 2024. [Online]. Available: https://markforged.com/3d-printers/mark-two.
[46] Zeybek MK, Güden M, Taşdemirci A. The effect of strain rate on the compression behavior of additively manufactured short carbon Fiber-reinforced polyamide composites with different layer heights, infill patterns, and built angles. J Mater Eng Perform Dec. 2023;32(24):11050–63. https://doi.org/10.1007/s11665-023-07918-1.
[47] Markforged, "Material specifications." Accessed: July 09, 2024. [Online]. Available: https://support.markforged.com/portal/s/article/Onyx.
[48] Pascual-González C, Iragi M, Fernández A, Fernández-Blázquez JP, Aretxabaleta L, Lopes CS. An approach to analyse the factors behind the micromechanical response of 3D-printed composites. Compos Part B Eng Apr. 2020;186:107820. https://doi.org/10.1016/j.compositesb.2020.107820.
[49] Vision Research. Phantom camera control 3.11.11. Phantom; 2024.
[50] ASTM, "ASTM D7136/D7136M: standard test method for measuring the damage resistance of a Fiber-reinforced polymer matrix composite to a drop-weight impact event." Accessed: Apr. 17, 2024. [Online]. Available: https://compass.astm.org/document/?contentCode=ASTM%7CD7136_D7136M-15%7Cen-US&proxycl=https%3A%2F%2Fsecure.astm.org&fromLogin=true.
[51] Li H, Chen W, Hao H. Factors influencing impact force profile and measurement accuracy in drop weight impact tests. Int J Impact Eng Nov. 2020;145:103688. https://doi.org/10.1016/j.ijimpeng.2020.103688.
[52] Novak N, et al. Impact loading of additively manufactured metallic stochastic sheet-based cellular material. Int J Impact Eng Apr. 2023;174:104527. https://doi.org/10.1016/j.ijimpeng.2023.104527.
[53] Alhembar A, Barsoum I, Scarpa F. On the correlation between static and dynamic mechanical properties in architected lattice materials. Mater Des Aug. 2025;256: 114315. https://doi.org/10.1016/j.matdes.2025.114315.
[54] Eren Z, Burnett CA, Wright D, Kazancı Z. Compressive characterisation of 3D printed composite materials using continuous fibre fabrication. Int J Lightweight Mater Manuf Dec. 2023;6(4):494–507. https://doi.org/10.1016/j.ijlmm.2023.05.002.
[55] Maskery I, Aremu AO, Parry L, Wildman RD, Tuck CJ, Ashcroft IA. Effective design and simulation of surface-based lattice structures featuring volume fraction and cell type grading. Mater Des Oct. 2018;155:220–32. https://doi.org/10.1016/j.matdes.2018.05.058.
[56] Maskery I, Aboulkhair NT, Aremu AO, Tuck CJ, Ashcroft IA. Compressive failure modes and energy absorption in additively manufactured double gyroid lattices. Addit Manuf Aug. 2017;16:24–9. https://doi.org/10.1016/j.addma.2017.04.003.
[57] Mulholland T, Goris S, Boxleitner J, Osswald TA, Rudolph N. Fiber orientation effects in fused filament fabrication of air-cooled heat exchangers. JOM Mar. 2018; 70(3):298–302. https://doi.org/10.1007/s11837-017-2733-8.
[58] Hou Y, Panesar A. Effect of manufacture-induced interfaces on the tensile properties of 3D printed polyamide and short carbon fibre-reinforced polyamide composites. Polymers (Basel) 2023;15(3):773. https://doi.org/10.3390/polym15030773.
[59] Su N, Pierce RS, Rudd C, Liu X. Comprehensive investigation of reclaimed carbon fibre reinforced polyamide (rCF/PA) filaments and FDM printed composites. Compos Part B Eng Mar. 2022;233:109646. https://doi.org/10.1016/j.compositesb.2022.109646.
[60] Goh GD, Yap YL, Agarwala S, Yeong WY. Recent progress in additive manufacturing of Fiber reinforced polymer composite. Adv Mater Technol 2019;4 (1). https://doi.org/10.1002/admt.201800271. Art. no. 1.
[61] Liu X, Wada T, Suzuki A, Takata N, Kobashi M, Kato M. Understanding and suppressing shear band formation in strut-based lattice structures manufactured by laser powder bed fusion. Mater Des Feb. 2021;199:109416. https://doi.org/10.1016/j.matdes.2020.109416.
[62] Yoo D-J. Advanced porous scaffold design using multi-void triply periodic minimal surface models with high surface area to volume ratios. Int J Precis Eng Manuf Aug. 2014;15(8):1657–66. https://doi.org/10.1007/s12541-014-0516-5.
[63] Mishra AK, Kumar A. Compression behavior of triply periodic minimal surface polymer lattice structures. Exp Mech Apr. 2023;63(4):609–20. https://doi.org/10.1007/s11340-023-00940-3.
[64] Bai L, Yi C, Chen X, Sun Y, Zhang J. Effective design of the graded strut of BCC lattice structure for improving mechanical properties. Materials (Basel) Jan. 2019; 12(13). https://doi.org/10.3390/ma12132192. Art. no. 13.
[65] Yang X, et al. Effect of volume fraction and unit cell size on manufacturability and compressive behaviors of Ni-Ti triply periodic minimal surface lattices. Addit Manuf June 2022;54:102737. https://doi.org/10.1016/j.addma.2022.102737.
[66] Wang X, et al. Inverse finite element modeling of the barreling effect on experimental stress-strain curve for high temperature steel compression test. J Mater Process Technol May 2017;243:465–73. https://doi.org/10.1016/j.jmatprotec.2017.01.012.
[67] Functionally graded porous scaffolds in multiple patterns: new design method, physical and mechanical properties. Mater Des Dec. 2018;160:849–60. https://doi.org/10.1016/j.matdes.2018.09.053.
[68] Maskery I, et al. Insights into the mechanical properties of several triply periodic minimal surface lattice structures made by polymer additive manufacturing. Polymer (Guildf) Sept. 2018;152:62–71. https://doi.org/10.1016/j.polymer.2017.11.049.
[69] Lu J, Dong P, Zhao Y, Zhao Y, Zeng Y. 3D printing of TPMS structural ZnO ceramics with good mechanical properties. Ceram Int Jan. 2021;47. https://doi.org/10.1016/j.ceramint.2021.01.152.
[70] Yang L, et al. Insights into unit cell size effect on mechanical responses and energy absorption capability of titanium graded porous structures manufactured by laser powder bed fusion. J Mech Behav Biomed Mater Sept. 2020;109:103843. https://doi.org/10.1016/j.jmbbm.2020.103843.
[71] Maskery I, et al. Mechanical properties of Ti-6Al-4V selectively laser melted parts with body-centred-cubic lattices of varying cell size. Exp Mech Sept. 2015;55(7): 1261–72. https://doi.org/10.1007/s11340-015-0021-5.
[72] Vanaei H, El Magri A, Rastak M, Vanaei S, Vaudreuil S, Tcharkhtchi A. Numerical–Experimental analysis toward the strain rate sensitivity of 3D-printed nylon reinforced by short carbon Fiber. Materials (Basel) Dec. 2022;15. https://doi.org/10.3390/ma15248722.
[73] Ghabezi P, Flanagan T, Walls M, Harrison NM. Degradation characteristics of 3D printed continuous fibre-reinforced PA6/chopped fibre composites in simulated saltwater. Prog Addit Manuf Jan. 2025;10(1):725–38. https://doi.org/10.1007/s40964-024-00654-5.
[74] Al Hassanieh S, Alhantoobi A, Khan KA, Khan MA. Mechanical properties and energy absorption characteristics of additively manufactured lightweight novel re-entrant plate-based lattice structures. Polymers (Basel) Nov. 2021;13(22):3882. https://doi.org/10.3390/polym13223882.
[75] Sharma D, Hiremath SS. Bio-inspired repeatable lattice structures for energy absorption: experimental and finite element study. Compos Struct Mar. 2022;283: 115102. https://doi.org/10.1016/j.compstruct.2021.115102.
[76] Affdl JCH, Kardos JL. The Halpin-Tsai equations: a review. Polym Eng Sci 1976;16 (5):344–52. https://doi.org/10.1002/pen.760160512.
[77] Yan J, Demirci E, Gleadall A. 3D short fibre orientation for universal structures and geometries in material extrusion additive manufacturing. Addit Manuf May 2023; 69:103535. https://doi.org/10.1016/j.addma.2023.103535.
[78] Zhang X, Zhang K, Zhang B, Li Y, He R. Additive manufacturing, quasi-static and dynamic compressive behaviours of ceramic lattice structures. J Eur Ceram Soc Dec. 2022;42(15):7102–12. https://doi.org/10.1016/j.jeurceramsoc.2022.08.018.
[79] Ling C, Cernicchi A, Gilchrist MD, Cardiff P. Mechanical behaviour of additively-manufactured polymeric octet-truss lattice structures under quasi-static and dynamic compressive loading. Mater Des Jan. 2019;162:106–18. https://doi.org/10.1016/j.matdes.2018.11.035.
[80] Weeks JS, Ravichandran G. High strain-rate compression behavior of polymeric rod and plate Kelvin lattice structures. Mech Mater Mar. 2022;166:104216. https://doi.org/10.1016/j.mechmat.2022.104216.
[81] Shen CJ, Lu G, Yu TX. Investigation into the behavior of a graded cellular rod under impact. Int J Impact Eng Dec. 2014;74:92–106. https://doi.org/10.1016/j.ijimpeng.2014.02.015.
[82] Hazeli K, Babamiri BB, Indeck J, Minor A, Askari H. Microstructure-topology relationship effects on the quasi-static and dynamic behavior of additively manufactured lattice structures. Mater Des Aug. 2019;176:107826. https://doi.org/10.1016/j.matdes.2019.107826.
[83] Weeks JS, Ravichandran G. High strain-rate compression behavior of polymeric rod and plate Kelvin lattice structures. Mech Mater Mar. 2022;166:104216. https://doi.org/10.1016/j.mechmat.2022.104216.
[84] Magino N, Köbler J, Andrä H, Welschinger F, Müller R, Schneider M. Accounting for viscoelastic effects in a multiscale fatigue model for the degradation of the dynamic stiffness of short-fiber reinforced thermoplastics. Comput Mech Mar. 2023;71(3):493–515. https://doi.org/10.1007/s00466-022-02246-y.
[85] Yue L, Liu H, Cheng Z, Kan Q, Kang G. Dynamic crushing behavior of a novel bi-directional gradient lattice structure under axial and oblique impact loadings. Thin-Walled Struct May 2024;198:111697. https://doi.org/10.1016/j.tws.2024.111697.
[86] Hoy RS, Robbins MO. Strain hardening of polymer glasses: effect of entanglement density, temperature, and rate. J Polym Sci Part B Polym Phys Dec. 2006;44(24). https://doi.org/10.1002/polb.21012. Art. no. 24.
[87] Jacob G, Starbuck J, Fellers J, Simunovic S, Boeman R. Strain rate effects on the mechanical properties of polymer composite materials. J Appl Polym Sci Sept. 2004;94:296–301. https://doi.org/10.1002/app.20901.